PROCEEDINGS OF SCIENCE

PoS(ICRC2025)094

Characterizing Cosmic-Ray Nuclei with the RadMap Telescope using Neural Networks

---

Luise Meyer-Hetling,[a,b,*] **Martin J. Losekamm,**[a,b,c] **Stephan Paul**[a,b] **and Thomas Pöschl**[d]

[a] *Technical University of Munich, School of Natural Sciences, Garching, Germany*
[b] *Excellence Cluster ORIGINS, Garching, Germany*
[c] *Now at European Space Agency, Noordwijk, Netherlands*
[d] *European Organization for Nuclear Research (CERN), Geneva, Switzerland*

E-mail: `luise.meyer-hetling@tum.de`

Detailed knowledge of the radiation environment in space is an indispensable prerequisite for space missions in low Earth orbit and beyond. The RadMap Telescope is a compact radiation monitor that can characterize the radiation environment aboard spacecraft and determine the biologically relevant dose received by astronauts. Its main sensor is a tracking calorimeter made from 1024 scintillating-plastic fibers of alternating orientation and silicon photomultipliers. It allows the three-dimensional tracking and identification of cosmic-ray nuclei by measurement of their energy-deposition profiles. The properties of nuclei traversing the detector are reconstructed using a neural-network-based analysis framework. In this contribution, we describe the three consecutive convolutional networks that we use to determine the track parameters, charge, and initial kinetic energy of each nucleus as well as the challenges of a network-based analysis approach. We demonstrate the capabilities of our framework with networks trained and evaluated on simulated data and show that the achieved performance is in agreement with the requirements of radiation monitoring. Finally, we discuss the significance of our results and the limitations of both the analysis framework and the detector.

39th International Cosmic Ray Conference (ICRC2025)
15–24 July 2025
Geneva, Switzerland

ICRC 2025
The Astroparticle Physics Conference
Geneva July 15-24, 2025

---

[*] Speaker

1. The Space Radiation Environment and its Effects on the Human Body

A thorough understanding of the space radiation environment —including its spectral, temporal, and spatial variations— is imperative for future space missions [4]. The main components of the radiation environment are solar energetic particles (SEP) and galactic cosmic rays (GCR). 98% of GCR are fully ionized nuclei of all naturally occurring elements. This nuclear component of GCR is made up of 87% protons, 12% helium nuclei, and 1% heavier nuclei [8]. During a solar particle event, bursts of SEP (mostly protons and light nuclei) pose a quasi-instantaneous threat to astronauts [11, 12]. In low Earth orbit, the Van Allen radiation belts are a third major component of the radiation environment. The impacts of this complex radiation field on the human organism comprise short- and long-term health risks, including acute radiation sickness, cancer [4, 9], cardiovascular diseases [5, 13], and impaired cognitive functions [2, 7, 10]. Most operational radiation monitors measure either only the linear energy transfer or the total energy deposition and are thus not able to determine the charge and energy of individual particles. The detector at the heart of our instrument is able to track traversing particles, differentiate between nuclei of different charge, Z, and measure their kinetic energy, E_{kin}. A first prototype was deployed to the International Space Station (ISS) between April 2023 and January 2024 for an in-orbit demonstration of its capabilities. We present the neural networks used to reconstruct particle properties and show their best-case performance using simulated data for both training and testing. We also discuss the limitations of our analysis framework.

2. The RadMap Telescope and its Measurement Principle

The central detector of the RadMap Telescope, the Active Detection Unit (ADU) consists of 1024 scintillating-plastic fibers with a square cross-section of $2\,\mathrm{mm} \times 2\,\mathrm{mm}$. They are arranged in a stack of 32 layers of alternating orientation (Figure 1). The scintillation light created by a traversing particle is detected using silicon photomultipliers (SiPMs) attached to one end of each fiber. This layout permits to reconstruct a particle's track through the detector with omnidirectional acceptance and record its energy-deposition profile along the track. The coordinate system used to parametrize the track's direction and orientation is given in Figure 1, with $\phi \in [-180°, 180°)$ and $\theta \in [0°, 180°]$. Additionally, the figure illustrates the two projections of signal amplitudes along the fiber orientations into the yx- and yz-planes that constitute the detector's data output.

For stopping particles, the measured energy-deposition profiles contain all the information required to determine their charge and energy. The corresponding reconstruction method, called *Bragg curve spectroscopy*, was first described by Gruhn et al. [6]. While a stopping particle's E_{kin} can be calculated as the integral of the energy-deposition profile, its charge can be inferred from the height of the Bragg peak. We can extend this measurement principle to through-going particles by deriving Z and the velocity β from the recorded energy deposition profile. The kinetic energy can then be determined from these quantities assuming an average atomic mass.

As we ultimately want our instruments to perform dosimetry measurements in near-real time, the reconstruction of each event's track, charge, and energy must be performed with short execution times. We thus opted for a framework consisting of three sequentially applied convolutional neural

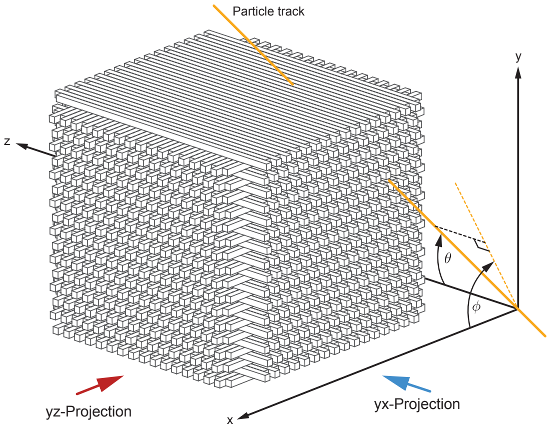

Figure 1: Schematic representation of the RadMap Telescope's central detector. Shown are the coordinate system and the spherical coordinates ϕ and θ we use to parametrize the orientation of particle tracks in the detector. The red and blue arrows indicate the two-dimensional projections we use to visualize and analyze the detector's data.

networks trained on simulated interactions of cosmic ray nuclei with the ADU. All three networks have a similar core architecture. In order to account for the different possible track lengths and thus the sizes of the structures we are trying to detect, we use inception layers that comprise multiple convolutional layers with different filter sizes in parallel [14]. The networks can thus learn by themselves which initial scale is best suited to find the patterns we are looking for in the training data.

We generated the data used for training, evaluation, and testing of the networks with the GEANT4 simulation toolkit [1, 3]. The physical processes from the standard physics list FTFP_BERT were extended by detector-specific effects like ionization quenching. The simulated detector model consisted of the scintillating-plastic fibers only. Any additional components —like the housing, read-out electronics and external shielding by the space station— were intentionally omitted to demonstrate the unbiased capabilities of the instrument. We only simulated the hadronic component of cosmic rays using the stable, most abundant isotopes of all naturally occurring elements from hydrogen to iron. The charge and energy distributions of the incident particles were chosen to optimize the performance of the trained networks and to reduce possible training biases from the training data. We thus did not model the space radiation environment realistically —with abundances differing by several orders of magnitude— but assumed all elements to be equally common. For E_{kin}, we used a log-uniform distribution with task-specific energy ranges instead of the GCR power-law spectrum to not introduce a significant bias towards lower energies. The nuclei were created on a spherical surface surrounding the detector, with an isotropic incident flux. Unless stated otherwise, we selected events for which a particle was detected in at least three fibers of each orientation ($N_{\text{sig}}^{yx} \geq 3$ and $N_{\text{sig}}^{yz} \geq 3$) to ensure they could be reconstructed.

3. Track Reconstruction

We aim to reconstruct ϕ and θ to parametrize a particle's path through the detector. In principle, full track reconstruction would also require to determine the position of the track. For our application, we are, however, primarily interested in the angular distribution of the incident particles. While ϕ can be read off the yx-plane, only the projection of θ, θ_{proj}, can be determined in the yz-plane. θ can be calculated from the two using $\theta = \arctan\left(\frac{\tan\theta_{\text{proj}}}{\sin\phi}\right)$. The neural network that we use for track reconstruction performs a dual classification task to provide us with two pseudo-probability distributions, one for ϕ and one for θ_{proj}, with a binning resolution of 0.2°. Here, we require a more restrictive event selection than specified above, with $N_{\text{sig}}^{yx} \geq 5$ and $N_{\text{sig}}^{yz} \geq 5$. In addition, at least one fiber in the central cuboid (24 layers × 24 fibers × 24 fibers) has to carry a signal in order for an event to be selected.

We assessed the capabilities of the network architecture on three different data sets. The first consisted of protons stopping in the detector. The second contained only protons with a kinetic energy of 120 MeV; the particles did not stop in the detector but their energy-deposition densities increased strongly along their track. The third set contained minimum ionizing particles (MIPs), again protons, with an energy of 3 GeV. The networks were trained on 0.9 million events. For each case, we determined the network's performance by calculating the classification accuracy, defined as the fraction of reconstructed angles that were assigned to the correct angle class by the respective network. For evaluation, the classification bins of width 0.2° are combined to form bins of width 1°. If the 1°-bin reconstructed by the network coincides with the true 1°-bin, an event is assigned as correctly classified. Figure 2 shows the resulting distributions as a function of the true angles.

For through-going protons (blue), we reach accuracies between 30% and 40% over almost the full angle range for both angles. Noticeable dips in the accuracy are visible for all $\phi \approx n \times 180°, n \in \mathbb{Z}$, and $\theta \approx 90°$. In the first case, protons travel mainly through a single layer of detector fibers, thus creating a signal in only one of the two detector projections (see Figure 1). As our selection cuts for reconstructable events require both $N_{\text{sig}}^{yx} > 0$ and $N_{\text{sig}}^{yz} > 0$, the corresponding events are heavily underrepresented in the training data, leading to a negative bias in the network's performance. In the second case, $\theta \approx 90°$ implies that the proton's track is parallel to the yx-plane. If in addition $\phi \approx n \times 180°, n \in \mathbb{Z}$, this entails a smaller number of hit fibers from the yz-projection, reducing the number of data points for the reconstruction of θ_{proj}. As these geometric observations are independent of the protons' energy, the overall shape of the distributions is the same for all three cases. Compared to through-going protons, the accuracies are overall lower for stopping protons (red curve in Figure 2) and particularly for MIPs (yellow curve in Figure 2). The event signatures of stopping protons on average contain a smaller number of fibers with signal, thus providing fewer data points for the track reconstruction. For MIPs, for which the energy-deposition density changes very little along their path through the detector, the network is able to correctly determine the orientation of their tracks but not the direction in which the particle is traveling. This translates into a notable fraction of events for which the reconstructed ϕ is off by 180°. Consequently, the corresponding accuracy for ϕ is reduced by a factor of two compared to the case of monoenergetic, through-going particles.

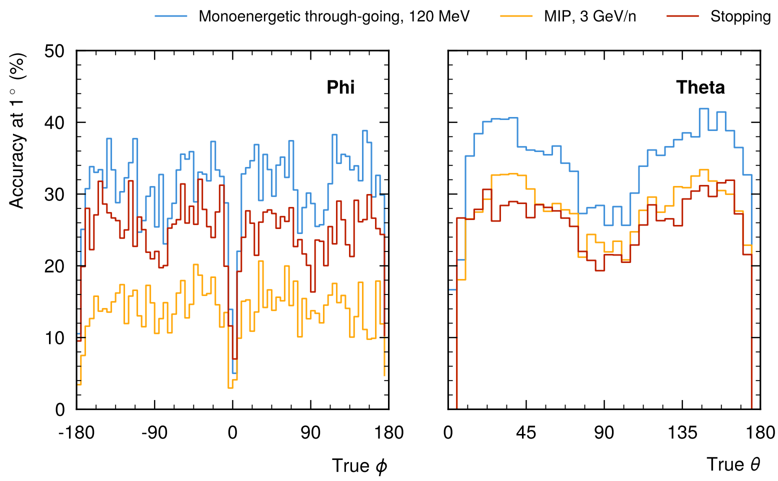

Figure 2: Reconstruction accuracy of the track angles ϕ (left) and θ (right) for protons as a function of the true angles. We define the accuracy as the fraction of the testing events that was correctly assigned to the true angle bin of width 1°.

4. Charge Determination

By measuring specific energy-deposition profiles, the ADU can determine the charge of incident particles. As we assume the primary particles to be fully-ionized nuclei and as the mass number, A, has a noticeable effect only on the lightest nuclei, determining their charge is sufficient to unambiguously identify them. Efficiently detecting light nuclei —particularly protons and helium— is of high interest for radiation dosimetry. The abundance of these elements in cosmic rays is orders of magnitude higher than that of heavier elements such that they contribute strongly to the absorbed dose. Iron as the heaviest naturally occurring element is the second significant contributor due to its high biological effectiveness. We thus developed an analysis framework that can resolve small Z with high resolution while still reaching acceptable performances for higher Z by performing a two-step charge determination. It consists of a first network trained to identify nuclei from hydrogen to oxygen, which passes on all higher Z to a second network specifically trained to recognize fluorine through iron. Both networks have the same architecture and were trained with nine million training events (two million of them being used for evaluation). To avoid boundary effects for iron nuclei, the training data set of the second network also included cobalt nuclei. The energy range of the incident nuclei was 20 MeV to 5 TeV.

The combined identification performance of the two networks is summarized in Figure 3. In this confusion matrix, each column contains the distribution of reconstructed nuclear charges, Z_{rec}, for all events with true nuclear charge Z_{mc}. The framework correctly identifies hydrogen (protons) and helium in 99.8% and 99.3% of events, respectively. For all lighter ions up to oxygen, values well over 95% can be achieved. For heavier nuclei, the exact charge determination evidently becomes more difficult. This observation is in agreement with the fact that the effects leading to deviations from the ideal energy-deposition profile become stronger for increasing Z. However, in most cases,

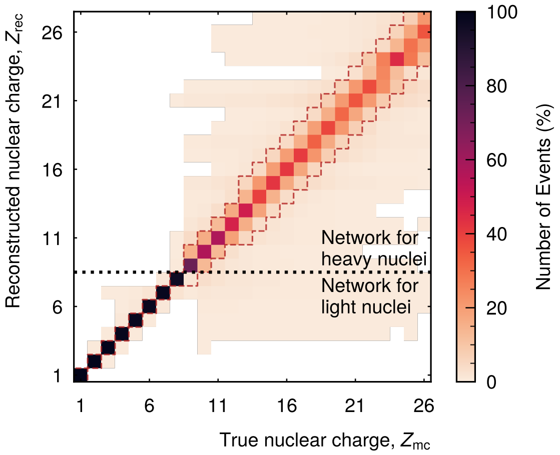

Figure 3: Confusion matrix of the charge determination performed by the consecutive application of two neural networks, trained to identify low-charge nuclei through oxygen ($Z = 8$) and high-charge nuclei through iron ($Z = 26$), respectively. The dashed red line illustrates the range containing 80% of Z_{rec} for each Z_{mc}. Cells with values smaller than 0.1% are masked, i.e., drawn in white.

the network assigns the largest fraction of events to the correct class and learns to roughly recognize the energy-deposition profiles of nuclei with larger Z. If we require an accuracy larger than 80% (red dashed line), we have to allow $|\Delta Z| \leq 1$ for fluorine to magnesium and $|\Delta Z| \leq 2$ for aluminum to iron. This uncertainty caused by the reduced charge resolution is still much smaller than for a determination of Z from the LET alone. Our measurement of the biologically relevant dose therefore outperforms that of the majority of sensors used today.

5. Energy Measurement

After determining the charge of the nuclei traversing the detector, we are able to reconstruct each E_{kin}. We trained 26 element-specific neural networks of identical architectures with 1.8 million events to determine E_{kin} based on the previously reconstructed Z. To take into account the Z-dependent purity of the data sets that are being passed on to the energy networks and to reduce the effect of incorrectly determined Z on the energy reconstruction, the individual training data sets do not only contain events of the target Z. Instead, they comprise events with charges in the range $[Z-1, Z+1]$ (lower Z) or $[Z-2, Z+2]$ (higher Z). For hydrogen, the network is trained on $Z = 1$ only. Depending on Z, the networks are trained on the energy range 20 MeV/n to 1 GeV/n or 20 MeV/n to 10 GeV/n.

Using a data set of eight million testing events, we evaluate the combined performance of the consecutive determination of Z and E_{kin}. Figure 4 exemplarily shows the energy resolution for selected elements: hydrogen, helium, carbon, and iron. We calculate the resolution as the difference ΔE_{kin} between the reconstructed and the true E_{kin} divided by the true E_{kin}. For helium and carbon, we trained the respective networks with nuclei in the range $[Z-1, Z+1]$ of the target charge, for iron with nuclei in the range $[Z-2, Z+2]$. The blue and yellow histograms allow a comparison

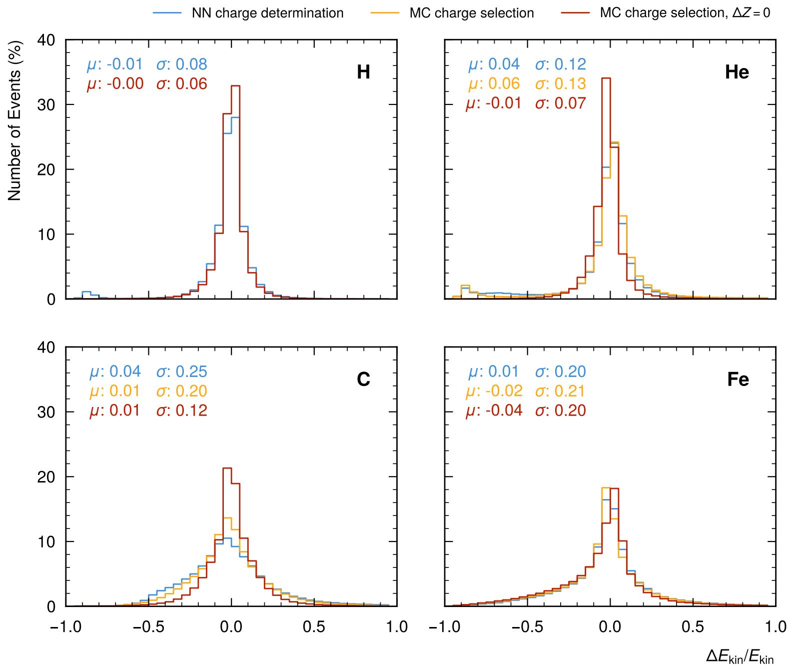

Figure 4: Energy resolution for hydrogen (H), helium (He), carbon (C), and iron (Fe) nuclei with energies from 20 MeV/n to 1 GeV/n (10 GeV/n for iron). The resolution is given as the difference ΔE_{kin} of reconstructed and true E_{kin}, normalized by the true E_{kin}. We additionally indicate the mean, μ, and the half-width of the 68%-interval, σ, for each distribution.

between the performance for events with manually selected Z (yellow) and events that were assigned to a given Z by our charge-determination network (blue). The red histograms additionally show an ideal energy-reconstruction performance that was obtained by training the networks on the target charge only ($\Delta Z = 0$) and manually selecting testing events with the correct Z for each network.

For each element, the distributions of $\Delta E_{\mathrm{kin}}/E_{\mathrm{kin}}$ are well centered around 0, having no significant bias. All three cases perform best for protons ($\sigma_{\mathrm{nn}} = 0.08$ and $\sigma_{\mathrm{mc}} = 0.06$), while the distributions become broader with increasing Z, as one would expect from Z-dependent effects like straggling, fragmentation, and quenching. The ideal case of $\Delta Z = 0$ generally performs best with standard deviations from 0.06 for protons to 0.12 for carbon. Although the Z-purity of the data sets passed on by the charge-determination framework heavily decreases with increasing Z, the use of $\Delta Z > 0$ in the training of the energy networks allows to compensate for this effect to some degree. For the example elements shown here, the impact of charge confusion is smallest for protons, for which our charge determination performs best, increases with Z, and is highest for carbon.

6. Conclusion

Our findings demonstrate that the RadMap Telescope can perform spectroscopic measurements that significantly exceed the capabilities of most instruments used for radiation monitoring aboard spacecraft today. They also show that acceptable results can be produced using a neural-network-based reconstruction framework. Further improvements of both our reconstruction results and their relevance to future applications can potentially be obtained by optimizing the network architectures and the training data, e.g., by using a more realistic model of the space radiation environment in our simulations.

References

[1] S. Agostinelli, J. Allison, et al. Geant4—a simulation toolkit. *Nuclear Instruments and Methods in Physics Research Section A: Accelerators, Spectrometers, Detectors and Associated Equipment*, 506(3):250–303, 2003.

[2] Y. Alaghband, P. M. Klein, et al. Galactic cosmic radiation exposure causes multifaceted neurocognitive impairments. *Cellular and Molecular Life Sciences*, 80(1):29, 2023.

[3] J. Allison, K. Amako, et al. Recent developments in Geant4. *Nuclear Instruments and Methods in Physics Research Section A: Accelerators, Spectrometers, Detectors and Associated Equipment*, 835:186–225, 2016.

[4] J. C. Chancellor, G. Scott, and J. Sutton. Space Radiation: The Number One Risk to Astronaut Health beyond Low Earth Orbit. *Life*, 4:491–510, 2014.

[5] M. D. Delp, J. M. Charvat, et al. Apollo Lunar Astronauts Show Higher Cardiovascular Disease Mortality: Possible Deep Space Radiation Effects on the Vascular Endothelium. *Scientific Reports*, 6:29901, 2016.

[6] C. Gruhn, M. Binimi, et al. Bragg curve spectroscopy. *Nuclear Instruments and Methods in Physics Research*, 196:33–40, 1982.

[7] P. M. Klein, V. K. Parihar, G. G. Szabo, et al. Detrimental impacts of mixed-ion radiation on nervous system function. *Neurobiology of Disease*, 151:105252, 2021.

[8] M. S. Longair. *High Energy Astrophysics*. Cambridge University Press, Cambridge, 2012.

[9] National Academies of Sciences, Engineering, and Medicine. *Space Radiation and Astronaut Health: Managing and Communicating Cancer Risks*. The National Academies Press, Washington, DC, 2021.

[10] V. K. Parihar, B. Allen, K. K. Tran, et al. What happens to your brain on the way to Mars. *Science Advances*, 1:e1400256, 2015.

[11] D. V. Reames. *Solar Energetic Particles*. Lecture Notes in Physics. Springer, Cham, 2021.

[12] D. V. Reames. Energy Spectra vs. Element Abundances in Solar Energetic Particles and the Roles of Magnetic Reconnection and Shock Acceleration. *Solar Physics*, 297(3), 2022.

[13] R. Rikhi, G. Samra, et al. Radiation induced cardiovascular disease: An odyssey of bedside-bench-bedside approach. *Life Sciences in Space Research*, 27:49–55, 2020.

[14] C. Szegedy, W. Liu, et al. Going deeper with convolutions. In *2015 IEEE Conference on Computer Vision and Pattern Recognition (CVPR)*, Boston, MA, 2015. IEEE.